

Scaler Mode Technique for the ARGO-YBJ Detector

The Argo-YBJ Collaboration:

G. Aielli ^{a,b}, C. Bacci ^{c,d}, F. Barone ^{e,f}, B. Bartoli ^{g,f},
P. Bernardini ^{h,i}, X.J. Bi ^j, C. Bleve ^{h,i,1}, P. Branchini ^d,
A. Budano ^d, S. Bussino ^{c,d}, A.K. Calabrese Melcarne ^{h,i},
P. Camarri ^{a,b}, Z. Cao ^j, A. Cappa ^{k,ℓ}, R. Cardarelli ^b,
S. Catalanotti ^{g,f}, C. Cattaneo ^m, S. Cavaliere ^{g,f}, P. Celio ^{c,d},
S.Z. Chen ^j, N. Cheng ^j, P. Creti ⁱ, S.W. Cui ⁿ, G. Cusumano ^{o,p},
B.Z. Dai ^q, G. D'Alí Staiti ^{p,r}, Danzengluobu ^s, M. Dattoli ^{k,ℓ,t},
I. De Mitri ^{h,i}, R. De Rosa ^{g,f}, B. D'Ettorre Piazzoli ^{g,f},
M. De Vincenzi ^{c,d}, T. Di Girolamo ^{g,f}, X.H. Ding ^s,
G. Di Sciascio ^f, C.F. Feng ^u, Zhaoyang Feng ^j, Zhenyong Feng ^v,
C. Ferrigno ^{o,p}, F. Galeazzi ^d, P. Galeotti ^{k,t}, X.Y. Gao ^q,
R. Gargana ^d, F. Garufi ^{g,f}, Q.B. Gou ^j, H.H. He ^j, Haibing Hu ^s,
Hongbo Hu ^j, Q. Huang ^v, M. Iacovacci ^{g,f}, I. James ^{m,w},
H.Y. Jia ^v, Labaciren ^s, H.J. Li ^s, J.Y. Li ^u, B. Liberti ^b,
G. Liguori ^{m,w}, C.Q. Liu ^q, J. Liu ^q, H. Lu ^j, G. Mancarella ^{h,i},
S.M. Mari ^{c,d}, G. Marsella ^{i,x}, D. Martello ^{h,i}, S. Mastroianni ^{c,d},

X.R. Meng^s, J. Mu^q, L. Nicastro^{p,y}, C.C. Ning^s,
 L. Palummo^{a,b}, M. Panareo^{i,x}, L. Perrone^{i,x}, P. Pistilli^{c,d},
 X.B. Qu^u, E. Rossi^f, F. Ruggieri^d, L. Saggese^{g,f}, P. Salvini^m,
 R. Santonico^{a,b}, A. Segreto^{o,p}, P.R. Shen^j, X.D. Sheng^j,
 F. Shi^j, C. Stanescu^d, A. Surdoⁱ, Y.H. Tan^j, P. Vallania^{k,ℓ,*},
 S. Vernetto^{k,ℓ}, C. Vigorito^{k,t}, H. Wang^j, Y.G. Wang^j,
 C.Y. Wu^j, H.R. Wu^j, B. Xu^v, L. Xue^u, H.T. Yang^q,
 Q.Y. Yang^q, X.C. Yang^q, G.C. Yu^v, A.F. Yuan^s, M. Zha^j,
 H.M. Zhang^j, J.L. Zhang^j, L. Zhang^q, P. Zhang^q,
 X.Y. Zhang^u, Y. Zhang^j, Zhaxisangzhu^s, X.X. Zhou^v,
 F.R. Zhu^j, Q.Q. Zhu^j G. Zizzi^{h,i}

^a*Dipartimento di Fisica dell'Università "Tor Vergata" di Roma, via della Ricerca Scientifica 1, 00133 Roma, Italy*

^b*Istituto Nazionale di Fisica Nucleare, Sezione di Tor Vergata, via della Ricerca Scientifica 1, 00133 Roma, Italy*

^c*Dipartimento di Fisica dell'Università "Roma Tre" di Roma, via della Vasca Navale 84, 00146 Roma, Italy*

^d*Istituto Nazionale di Fisica Nucleare, Sezione di Roma3, via della Vasca Navale 84, 00146 Roma, Italy*

^e*Dipartimento di Scienze Farmaceutiche dell'Università di Salerno, via Ponte Don Melillo, 84084 Fisciano (SA), Italy*

^f*Istituto Nazionale di Fisica Nucleare, Sezione di Napoli, Complesso Universitario di Monte Sant'Angelo, via Cinthia, 80126 Napoli, Italy*

- ^g*Dipartimento di Fisica dell'Università di Napoli, Complesso Universitario di Monte Sant'Angelo, via Cinthia, 80126 Napoli, Italy*
- ^h*Dipartimento di Fisica dell'Università di Lecce, via Arnesano, 73100 Lecce, Italy*
- ⁱ*Istituto Nazionale di Fisica Nucleare, Sezione di Lecce, via Arnesano, 73100 Lecce, Italy*
- ^j*Key Laboratory of Particle Astrophysics, Institute of High Energy Physics, Chinese Academy of Science, P.O. Box 918, 100049 Beijing, P.R. China*
- ^k*Istituto Nazionale di Fisica Nucleare, Sezione di Torino, via P.Giuria 1 - 10125 Torino, Italy*
- ^l*Istituto di Fisica dello Spazio Interplanetario dell'Istituto Nazionale di Astrofisica, corso Fiume 4 - 10133 Torino, Italy*
- ^m*Istituto Nazionale di Fisica Nucleare Sezione di Pavia, via Bassi 6, 27100 Pavia, Italy*
- ⁿ*Hebei Normal University, Shijiazhuang 050016, Hebei, China*
- ^o*Istituto di Astrofisica Spaziale e Fisica Cosmica di Palermo, Istituto Nazionale di Astrofisica, Via Ugo La Malfa 153 - 90146 Palermo, Italy*
- ^p*Istituto Nazionale di Fisica Nucleare, Sezione di Catania, Viale A. Doria 6 - 95125 Catania, Italy*
- ^q*Yunnan University, 2 North Cuihu Rd, 650091 Kunming, Yunnan, P.R. China*
- ^r*Università degli Studi di Palermo, Dipartimento di Fisica e Tecnologie Relative, Viale delle Scienze, Edificio 18 - 90128 Palermo, Italy*
- ^s*Tibet University, 850000 Lhasa, Xizang, P.R. China*
- ^t*Dipartimento di Fisica Generale dell'Università di Torino, via P.Giuria 1 - 10125 Torino, Italy*
- ^u*Shandong University, 250100 Jinan, Shandong, P.R. China*

^v*South West Jiaotong University, 610031 Chengdu, Sichuan, P.R. China*

^w*Dipartimento di Fisica Nucleare e Teorica dell'Università di Pavia, via Bassi 6,
27100 Pavia, Italy*

^x*Dipartimento di Ingegneria dell'Innovazione, Università di Lecce, 73100 Lecce,
Italy*

^y*Istituto di Astrofisica Spaziale e Fisica Cosmica di Bologna, Istituto Nazionale di
Astrofisica, Via Gobetti 101 - 40129 Bologna, Italy*

Abstract

The ARGO-YBJ experiment has been designed to study the Extensive Air Showers with an energy threshold lower than that of the existing arrays by exploiting the high altitude location (4300 m a.s.l. in Tibet, P.R. China) and the full ground plane coverage. The lower energy limit of the detector ($E \sim 1$ GeV) is reached by the scaler mode technique, i.e. recording the counting rate at fixed time intervals. At these energies, transient signals due to local (e.g. Forbush Decreases) and cosmological (e.g. Gamma Ray Bursts) phenomena are expected as a significant variation of the counting rate compared to the background. In this paper the performance of the ARGO-YBJ detector operating in scaler mode is described and discussed.

Key words: Cosmic Rays, Gamma Ray Bursts, Resistive Plate Chambers, Air Shower Arrays, Extensive Air Showers

PACS: 96.40.Pq, 98.70.Rz, 98.70.Sa

* corresponding author

Email address: `Piero.Vallania@to.infn.it` (P. Vallania).

¹ Presently at School of Physics and Astronomy, University of Leeds, Leeds, United Kingdom

1 Introduction

The study of gamma ray sources in the 1 - 100 GeV energy range has so far been only partially covered by observations by the satellite-based EGRET, with a maximum detectable energy of 30 GeV. On the other hand, present ground-based detectors such as Cherenkov Telescopes are still trying to reduce their threshold to energies well lower than 100 GeV.

In this energy range, Gamma Ray Bursts (GRBs) are certainly the most intriguing transient phenomena. GRBs have been deeply studied in the keV-MeV energy range, but only EGRET, in the last decade, provided some information in the GeV range. Three bursts have been detected at energies >1 GeV, with one photon of $E=18$ GeV [1,2]. The study of the high energy emission of GRBs could provide extremely useful constraints to the emission models and the parameters of the surrounding medium.

The interest for transient emission in the GeV region is not only restricted to extragalactic phenomena such as GRBs but also includes events closer to us - inside our Solar System - such as gamma rays from Solar Flares or high energy solar protons producing short time increases of the detector counting rate at the ground (Ground Level Enhancements).

The study of these transient phenomena can be successfully performed by ground-based experiments such as Extensive Air Shower (EAS) detectors working in “single particle mode” [3]. EAS arrays usually detect air showers generated by cosmic rays of energy $E \geq (1 - 100)$ TeV; the arrival direction of the primary particle is measured by the time delay of the shower front in different counters, and the primary energy is evaluated by the number of secondary particles detected.

EAS arrays can work in the energy region $E < 1$ TeV operating in single particle mode, i.e. counting all the particles hitting the individual detectors, independently of whether they belong to a large shower or they are the lone survivors of small showers. Because of the cosmic ray spectrum steepness, most of the events detected with this technique are in fact due to solitary particles from small showers generated by $1 - 100$ GeV cosmic rays.

Working in single particle mode, an air shower array could in principle detect a transient emission in the interval $1 - 100$ GeV (both by gamma rays or charged primaries) if the secondary particles generated by the primaries give a statistically significant excess of events over the background due to cosmic rays.

The power of this technique is in its extreme simplicity: it is sufficient to count all the particles hitting the detectors during fixed time intervals (i.e. every second or more frequently, depending on the desired time resolution) and to study the counting rate behaviour versus time, searching for significant increases. The observation of an excess in coincidence with a GRB detected by a satellite would be an unambiguous signature of the nature of the signal. The single particle technique does not allow one to measure energy and direction of the primary gamma rays, because the number of detected particles (often only one per shower) is too small to reconstruct the shower parameters. However, it can allow to study the temporal behaviour of the high energy emission, and, with some assumptions on the spectral slope (possibly supported by satellite measurements at lower energies), can give an evaluation of the total power emitted.

The background rate depends on the altitude and, to a lesser extent, on the geomagnetic latitude; it is not strictly constant and several effects both environmental and instrumental are responsible for variations on different time

scales with amplitudes up to a few per cent. For this technique, an accurate knowledge of the detector and its sensitivity to both environmental and instrumental parameters is of crucial importance in order to correctly evaluate the statistical significance of the detected signals.

Obviously the sensitivity of this technique increases with the detection area and the energy threshold decreases at higher observation levels, so the most suitable detectors have a large area and work at very high altitude.

The ARGO-YBJ experiment, located at the YangBaJing High Altitude Cosmic Ray Laboratory (Tibet, P.R. China, 4300 m a.s.l.) with a detection area of $\sim 6700 \text{ m}^2$, successfully exploits the full coverage approach at very high altitude with the aim of studying the cosmic radiation with a low energy threshold.

In order to cover many physics items in different energy ranges, two main operation modes have been designed: (1) shower mode, with an energy threshold of a few hundreds of GeV, and (2) scaler mode, with a threshold of a few GeV, this latter differing from the single particle mode for different particle multiplicities (i.e. not only the single particles) are put in coincidence and counted on different scaler channels.

The large field of view ($\gtrsim 2 \text{ sr}$, limited only by atmospheric absorption) and the high duty cycle (close to 100%) typical of EAS detectors, make ARGO-YBJ suitable to search for unknown sources and unpredictable events such as GRBs or other transient phenomena. The site location (latitude $30^\circ 06' 38''$ N, longitude $90^\circ 31' 50''$ E) allows sky monitoring in the declination band $-10^\circ < \delta < 70^\circ$.

In this paper the performance of ARGO-YBJ working in scaler mode will be described, with some examples of application of this technique in solar physics and in the search for GeV emission from GRBs.

2 The Detector

The ARGO-YBJ experiment is made by a single layer of Resistive Plate Chambers (RPCs) [4] housed in a large building ($100 \times 110 \text{ m}^2$). The detector has a modular structure: the basic module is a cluster ($5.7 \times 7.6 \text{ m}^2$), made of 12 RPCs ($2.850 \times 1.225 \text{ m}^2$ each). 130 of these clusters are organized in a full coverage carpet of 5600 m^2 with active area $\sim 93\%$; this central detector is surrounded by 23 additional clusters with a coverage of $\sim 40\%$ (“guard ring”) to improve the core location reconstruction. The installation of the central carpet was completed in June 2006.

Each RPC is read via 80 strips ($6.75 \times 61.80 \text{ cm}^2$), logically organized in 10 pads of $55.6 \times 61.8 \text{ cm}^2$ that are individually recorded and that represent the space-time pixels of the detector. The RPC carpet is connected to two different data acquisition systems, working independently, and corresponding to the two operation modes, shower and scaler. In shower mode, for each event the location and timing of every detected particle is recorded, allowing the lateral distribution and arrival direction reconstruction. In scaler mode the total counts are measured every 0.5 s: for each cluster, the signal coming from the 120 pads is added up and put in coincidence in a narrow time window (150 ns), giving the counting rates of ≥ 1 , ≥ 2 , ≥ 3 , ≥ 4 pads, that are read by four independent scaler channels. The corresponding measured counting rates are $\sim 40 \text{ kHz}$, $\sim 2 \text{ kHz}$, $\sim 300 \text{ Hz}$ and $\sim 120 \text{ Hz}$.

In order to correctly handle the data, it is very important to evaluate the response to particles hitting the detector. For scaler mode operations the most important parameters are the detector efficiency and the strip cross-talk, i.e., the probability of having adjacent pads fired by a single particle, giving false

coincident counts. These effects strongly depend on the adopted gas mixture and power supply (in our case Argon 15%, Isobutane 10% and Tetrafluoroethane 75% at 7200V). In these conditions a detector efficiency $\epsilon = 95\%$ has been measured together with a strip occupancy, i.e., the mean number of strips fired by a single particle, of 1.2 [4]. A very simple analytical calculation has been performed to evaluate the contribution of single particles to higher multiplicities: for the given strip occupancy, there is a probability of 10% for each strip to generate double counts. A “cross-talk region”, approximated for sake of simplicity to a step function, is defined as a width corresponding to 10% of the strip span. Taking into account the measured detection efficiency, the possibility of having cross-talk on both short and long strip sides, and the front-end digital logic - giving a maximum number of counts for each pad equal to 1 independently of the number of particles hitting simultaneously the pad - we obtain the following probabilities of measuring 0, 1 or 2 pads from a single particle hitting the RPC: $p(0) = 5\%$; $p(1) = 93\%$; $p(2) = 2\%$ (our analytical approximation does not give multiplicities greater than 2). This result has been checked experimentally on-site with one chamber, finding: $p(0) = 5.8\%$; $p(1) = 92.0\%$; $p(2) = 2.1\%$; $p(\geq 3) = 0.04\%$ [5]. The good agreement confirms the validity of our approach.

Finally, a substantially different behaviour is expected by the single particle channel (≥ 1) with respect to the higher multiplicity channels, because of the contributions given by spurious dark counts (related to front-end electronics and chamber noise) and natural radioactivity. Since from both we expect mostly single counts, these contributions should influence only the ≥ 1 scaler due to the very low rate of random coincidences. An on-site measurement to disentangle all these contributions to the single particle rate has been scheduled.

3 Detector Stability

Several effects are known to modify the background counting rate due to cosmic rays. First of all, variations in the atmospheric pressure affect the secondary particle flux: an increase (decrease) of the ground level atmospheric pressure results in a reduction (enhancement) of the background rate, because of the larger (smaller) absorption of the electromagnetic component. By monitoring the pressure at the detector position it is possible to correct the data for this effect. Local phenomena connected to the temperature and/or to the wind [6] at the level of the early shower development have also been measured, the effect being a change of the probability of secondary pions to decay with respect to their interaction, due to the local density variation. These effects are expected to be negligible compared to the above mentioned barometric effect, and very difficult to measure since the outdoor temperature, that is usually monitored, is weakly correlated to the high atmosphere ($\sim 10\text{ km}$) temperature. Moreover, the experiment hall temperature modifies the detector performance, changing the gas density inside the RPCs and the bakelite electrodes resistivity.

The cosmic ray background variations due to these parameters are not negligible (up to a few per cent of the counting rate in some cases), nevertheless for signals shorter than a few minutes (such as a high energy emission from a GRB) they can be neglected due to the very different time scales of the two phenomena. Much more troublesome are possible instrumental effects, such as electric noise, that could simulate a GRB signal producing spurious increases in the background rate. Working in single particle mode requires very stable detectors, and a very careful and continuous monitoring of the experimental

conditions. By comparing the counting rates of the scaler channels and requiring simultaneous and consistent variations in all of these, it is possible to identify and reject most of the noise events due to instrumental effects. In the following subsection the study of the detector behaviour over short time periods is discussed.

On the other hand, when the study involves long duration signals (as for solar activity or sidereal anisotropies) a correction to the counting rates is required in order to feature the underlying phenomena. The effects of our corrections for the atmospheric pressure and the hall temperature and their efficiency in shrinking the counting rate distributions towards a Poissonian distribution are discussed in section 3.2.

3.1 Detector stability over short time periods

We define as “short” a time period with a duration less than half an hour. Figs. 1 and 2 show the counting rates for multiplicities ≥ 1 , ≥ 2 , ≥ 3 , ≥ 4 and 1, 2, 3 for a typical cluster during 30 minutes of data acquisition. The counting rates C_i are obtained from the measured counting rates $C_{\geq i}$ using the relation:

$$C_i = C_{\geq i} - C_{\geq i+1} \quad (i = 1, 2, 3) \quad (1)$$

The distributions for all $C_{\geq i}$ and C_i are Poissonian, meaning that the environmental parameter variations have negligible effects over such a time scale. A useful variable is obtained by adding up counting rates of different multiplicities for the same cluster or different clusters for the same counting rate multiplicity. In this case, non-Poissonian behaviours appear due to the correlation between different channels. For the total number of particles hitting a

cluster we have:

$$C_{tot} = \sum_{i=1}^4 iC_i \simeq C_1 + 2C_2 + 3C_3 + 4C_{\geq 4} = C_{\geq 1} + C_{\geq 2} + C_{\geq 3} + C_{\geq 4} \quad (2)$$

Applying the error propagation to eq. (2) we obtain:

$$\sigma_{C_{tot}}^2 = \langle C_1 \rangle + 4\langle C_2 \rangle + 9\langle C_3 \rangle + 16\langle C_{\geq 4} \rangle \quad (3)$$

that is larger than a Poisson distribution. Fig. 3 shows the experimental distribution of the counting rate C_{tot} for the same cluster and time interval shown in figures 1 and 2. As expected, the distribution is Gaussian, wider than Poissonian and with a width $\sigma_{exp}=(223\pm 4)$ Hz, compatible with the value of (220 ± 6) Hz obtained by applying eq. (3).

More difficult to estimate is the correlation between different clusters due to the probability that some of the counts are generated by the same events giving the same multiplicity in different clusters. These events mean the counts in different clusters are not independent, widening the distribution from Poissonian with the sum of counts from more clusters. An analytical calculation gives the following result: if M_i is the counting rate of cluster i for a given multiplicity ($\geq 1, \geq 2, \geq 3, \geq 4$ or $1, 2, 3$) and n is the total number of clusters, we have:

$$M_{tot} = \sum_{i=1}^n M_i$$

$$\sigma_{M_{tot}}^2 = \langle M_{tot} \rangle \left(1 + \sum_{i=2}^n (i^2 - i)p_i \right) \quad (4)$$

where p_i is the probability that the multiplicity is satisfied for the same event on (and only on) i clusters. As an example, if we consider three clusters and multiplicity ≥ 1 , we can have two or three clusters hit by at least one particle

coming from the same shower. In this case, $p_3 = \frac{N_{123}}{M_{tot}}$ and $p_2 = \frac{N_{12}+N_{13}+N_{23}}{M_{tot}}$, where N_{123} is the number of counts generated by events hitting all the three clusters (with at least one particle) and N_{ij} by events hitting one couple of clusters. N_{ij} is not included in N_{123} : if three clusters are hit by the same event this contributes only to N_{123} .

The width of the M_{tot} distribution is larger than the Poissonian value $\sigma_{M_{tot}}^2 = \langle M_{tot} \rangle$; the p_i values depend on the given multiplicity, the EAS lateral distribution function and the cluster layout. Since the correlation between different clusters is topologically-dependent, for the same number of clusters and multiplicity we expect a wider distribution for close clusters compared to more distant ones. This has been checked experimentally. As the sensitivity of the scaler mode technique is inversely proportional to background fluctuations, a continuous carpet is at a disadvantage with respect to scattered detectors with the same total surface area.

The behaviour is the same for the distribution of the ratio between signal and background fluctuations (instead of the count rates), as in the GRB search analysis. Considering a number s of counts in a time interval Δt corresponding to the GRB duration and a background b of counts averaged on a time interval 10 times Δt before and after the signal, we define the normalized fluctuation function:

$$f = (s - b)/\sigma, \quad \sigma = \sqrt{b + b/20} \quad (5)$$

which represents the significance of the excess compared to background fluctuations.

Fig. 4 shows the f distribution for the same cluster of Figs. 1-3 and for $\Delta t = 10$ s, obtained using one day of data, for multiplicity ≥ 1 and for the sum

of the four multiplicities from ≥ 1 to ≥ 4 . Notice that for the single channel the Poissonian behaviour of the f distribution is preserved even if the total distribution is obtained with 24 hours of data, provided that the total time duration of signal plus background is less than 30 minutes. Since the value of f is calculated independently for each signal and background time intervals, the long term variations can be neglected and the single channel response is always “locally” Poissonian. On the contrary, the f distribution of the sum $\sum_{i=1}^4 C_{\geq i}$ follows equation (3), and the width of 1.07 can be easily obtained by using the experimental counting rates. The fact that the distribution of f is not affected by long term variations is also very useful to select good and bad channels, the latter showing very clearly anomalous non-Poissonian fluctuations.

3.2 Detector stability over long time periods and correlation with environmental parameters

As already stated at the beginning of this section, several effects are expected to modulate the counting rate measured by our RPC detector, affecting both the shower development and instrumental response. These effects must be corrected before any analysis of long term phenomena, i.e. with duration greater than ~ 30 minutes.

Changes in the atmospheric pressure (P) and the RPC temperature (T) are expected to dominate the count rate variations. The correlation with the atmospheric pressure has been widely studied, and a typical coefficient of $\approx 0.7\%/mbar$ is found for a very large range of primary energies [7]. At our atmospheric depth ($606 g cm^{-2}$), the vertical flux of soft (e) and hard (μ)

components are almost equivalent [8], reducing the dependency of the pressure correction coefficient on the atmospheric depth (i.e. zenith angle) due to the muonic component. The connection between the counting rates and the local temperature is mainly due to the anti-correlation of the bakelite electrode plates resistivity with the temperature [9,10]. In addition, a variation in the detector temperature modifies the gas density, causing a change in the effective gap width (the gas volume being constant): the final result is a direct correlation between the counting rate and the detector temperature, that we assume is the temperature of the gas just out of the RPC.

Fig.5 shows the counting rates for 3 clusters for multiplicities from ≥ 1 to ≥ 4 as a function of local solar time for 72 hours of data accumulation, together with the P and T behaviour. Besides the atmospheric pressure and the detector temperature, the solar diurnal anisotropy [11] is responsible for the counting rate modulation, while the differences in efficiency, chamber dark current and electronics noise give the offset displacements.

In order to correct for these effects we performed a fit with a two-dimensional function (as a first approximation linear in P, T) given by the following expression:

$$C(P, T) \simeq C_0[1 - \mu(P - P_0)][1 + \beta(T - T_0)] \quad (6)$$

where P_0 and T_0 are the reference values of pressure and temperature for counting rate C_0 , and μ and β are respectively the barometric and thermal coefficients. For the counting channel ≥ 1 we found a barometric coefficient $\mu = 0.3-0.5\%/mbar$ and a thermal coefficient $\beta = 0.2-0.4\%/^{\circ}C$, depending on the cluster considered and the specific experimental conditions. For the other scalars we obtain $\mu = 0.9-1.2\%/mbar$ and $\beta = 0.2-0.4\%/^{\circ}C$ [12].

Fig. 6 shows the counting rate distribution for $C_{\geq 1}$ and $C_{\geq 2}$ before and after corrections for the previous parameters in a period of 24 hours. It can be seen that for the counting channel ≥ 1 the corrected data becomes Gaussian but not yet Poissonian, with an experimental standard deviation 23% greater than the expected value. In contrast, the distribution of $C_{\geq 2}$ is Gaussian for the raw data and becomes Poissonian after corrections. The fact that the two raw distributions for the same day and the μ , β coefficients are completely different for $C_{\geq 1}$ and $C_{\geq 2}$ may be explained assuming that part of the $C_{\geq 1}$ counts are not due to cosmic rays.

The statistical behaviour of the counting rates after corrections for atmospheric pressure and RPC temperature has been checked for longer periods showing an agreement better than 5% up to 1 month for $C_{\geq 2}$ or higher scalars, while for $C_{\geq 1}$ the distribution becomes asymmetrical and much larger ($\sim 36\%$) than Poissonian already after 48 hours.

3.2.1 *The Forbush Decrease of January 2005*

An example of detection of a long-term phenomenon, linked to solar activity, is given by the Forbush Decrease (FD) observed in coincidence with the YBJ neutron monitor in January 2005. A FD is the fall in the cosmic ray intensity at the Earth one or more days after an Earth directed Coronal Mass Ejection (CME) lift-off, and is caused by the shielding effect of the magnetic field and shock associated with the high speed plasma cloud emitted from the Sun at the time of the eruption. Large solar flares can be associated with Ground Level Enhancements (GLEs) and, depending on the flare location, may also produce a CME that causes a FD; both of these phenomena are normally detected at the ground by neutron monitors, but a large area detector working

in scaler mode is also suitable.

The FD mentioned above was recorded by the worldwide network of neutron monitors as a significant decrease in the counting rate after a sudden storm commencement. The IGY neutron monitor at Jungfraujoch (Switzerland, vertical effective cut-off rigidity $R_c=4.5$ GV) observed a decrease with onset around noon UT on January 17, 2005, and with a maximum amplitude of about -15% [13]. On January 20, during the recovery phase of the FD at Earth, an X7.1 solar flare created a very intense burst of energetic particles and a GLE was observed, with onset time between 6:48 and 6:57 UT and maximum amplitude $> 5000\%$ at the South Pole neutron monitor station. The GLE spectrum was very soft, with a spectral index approaching asymptotically $\alpha \sim -5$ [14], producing quite small responses at even moderate geomagnetic cut-off rigidity locations like Jungfraujoch, where the maximum amplitude was 11.4%. FDs similarly produce an energy dependent drop in intensity deeper at low cut-off rigidity locations, but since their spectra are much harder than in GLEs they should be observable by the ARGO-YBJ array, characterized by $R_c=14$ GV [15]. Fig. 7 shows the YBJ neutron monitor data compared with the four counting rate distributions corrected only for the atmospheric pressure since the RPC temperature measurement was not yet implemented. Only 12 clusters were in operation at that time. Even if the scaler mode counting rate is more sensitive to environmental parameters, a correlation can be clearly seen, with an amplitude of -7% in the YBJ neutron monitor data and about -5% and -4% for $C_{\geq 1}$ and $C_{\geq 2}$ data. No decrease is observed for $C_{\geq 3}$ and $C_{\geq 4}$, and no GLE is seen in any scaler channel and in the YBJ neutron monitor data. Another interesting feature of FDs is the recovery phase. While the magnitude of FDs depends on the cut-off rigidity (as already shown), the recovery time is expected to be independent of the galactic cosmic ray energy and thus similar

for all detectors. Despite of this, as pointed out in [16], the recovery time in some events strongly depends on the median energy of the detected particles, with a faster recovery for more energetic cosmic rays. Moreover, these higher energy cosmic rays show an "over-recovery", i.e. a recovery of the cosmic ray intensity to a level higher than that before the FD. The study of these features is very important to characterize and model the propagation of the interplanetary shocks; due to its high cut-off rigidity, ARGO-YBJ can contribute to the study of acceleration processes, keeping in mind that the energy upper limit for incoming solar particles in the Earth environment has not yet been established. Due to its huge area, this study can be done with high sensitivity and small integration time. For example, a distinct enhancement of the diurnal variation in the recovery phase after the FD can be seen mainly around 24-25 January. It is most obvious in the $C_{\geq 2}$ data, but it is also evident in the $C_{\geq 3}$ and $C_{\geq 4}$ data where the FD is not observed. This phenomenon is known but not extensively studied, hence our data can give valuable information on the energy dependency of the FD recovery. A more detailed analysis of these data and their correlation is in progress.

4 Effective Area and Expected Counting Rates

The effective area is usually obtained by simulating a large number of showers N_{sim} with the core sampled on a wide area A_{sim} , much wider than typical shower dimensions, and counting the number of showers N_{trig} matching the trigger condition:

$$A_{eff}(E) = A_{sim} \cdot N_{trig}/N_{sim} \quad (7)$$

For the ARGO-YBJ detector, the effective area has been estimated by means of a detailed Monte Carlo (MC) simulation for photons, protons and helium of fixed energies ranging from 10 MeV to 100 TeV and fixed zenith angle θ from 0 to 50 degrees (with 10 degrees steps). The CORSIKA/QGSJet code 6.204 [17] has been used with a full electromagnetic component development down to $E_{thr} = 1$ MeV for electrons and photons and 50 MeV for muons and hadrons.

Since the actual efficiency depends essentially on the shower particle lateral distribution, a huge number of showers must be simulated over an area large enough to completely contain the event.

In order to save computing time the shower sampling has been performed by means of the “*reciprocity technique*” [18]: the sampling area A_S is uniformly filled with replicas of the same ARGO-YBJ carpet, one next to the other, for a total area of $\sim 10^4 \times 10^4 \text{ m}^2$. Following the reciprocity technique, we sample the shower axis only over the area covered by the carpet located at the center of the array, with the prescription of considering the response of all the detector replicas. Then, event by event, we calculate the number of clusters on the entire grid which contain at least 1, 2, 3, 4 fired pads. In this calculation the cross-talk between adjacent pads has been taken into account, as discussed in section 2. The resulting effective areas for the full ARGO-YBJ detector as a function of the energy of primary photons and protons at zenith angle $\theta = 20^\circ$ are shown in Fig. 8 in the four multiplicity channels (1, 2, 3 and ≥ 4).

If the probability that more than one particle per shower hits the detector is negligible, i.e. for sufficiently small detector and/or small primary energy, the effective area A_{scaler} scales like the mean electron size after the shower

maximum at the detection level [3]:

$$A_{scaler} \approx \epsilon \cdot \langle N_{Ch} \rangle \cdot A_d \cdot \cos \theta. \quad (8)$$

where ϵ and A_d are the detector efficiency and area, and $\langle N_{Ch} \rangle$ is the mean number of charged secondary particles. From Fig. 8 we see that, as expected, the dependence is described by a power law index ≈ 1.6 for multiplicity 1, and this index increases with the multiplicity approaching the value ≈ 2.6 , valid only in the shower trigger configuration [19]. The index lowers with increasing energy when the formula (8) loses its validity because the area of the cluster is too large for the given shower particle density and thus more than one particle fires it. The effective area for protons is usually lower than that for photons of the same energy, increasing the sensitivity of the measurement, except in the 10 – 100 GeV energy range, where, due essentially to the muonic component, the total number of charged particles in proton-induced showers is larger than that in photon events. Moreover, the geomagnetic cutoff at YBJ is ≥ 14 GV (depending on the arrival direction) [15].

In order to get the counting rates, the effective area is folded with the primary spectrum, expressed by a differential power law with spectral index $\alpha = -2.0$ for photons, $\alpha = -2.77$ for protons and $\alpha = -2.64$ for helium [20]. We adopted $\alpha = -2.0$, which is the mean spectral index for GRBs as measured by EGRET [21]. The resulting convolutions for photons and protons are shown in Fig. 9. The behaviour of these curves shows how each energy decade contributes to the counting rate for a fixed zenith angle. One can note that using four scalers instead of a single one allows the investigation of different energy ranges, with the possibility of giving an indication on the source spectral index in case of positive detection.

The resulting counting rates, integrating the different effective areas for angular bins up to a zenith angle of 60 degrees and both proton and helium contributions, are 24.4 kHz for C_1 , 1.8 kHz for C_2 , 195 Hz for C_3 and 117 Hz for $C_{\geq 4}$. The uncertainties on these rates come mainly from those affecting the primary fluxes which are estimated to be about 20% (see for example [22]). A comparison with the measured rates, i.e., 38 kHz for C_1 , 1.7 kHz for C_2 , 180 Hz for C_3 and 120 Hz for $C_{\geq 4}$, shows a very good agreement between the predicted values and the experimental, apart from the counting rate C_1 affected by spurious signals as explained in section 2.

5 Upper Limits and Expected Sensitivity

The energy fluence F in the energy range $[E_{min}, E_{max}]$ corresponding to an excess of N events above the cosmic ray background is given by:

$$F(\alpha, E_{max}) = \frac{N \int_{E_{min}}^{E_{max}} E^{\alpha+1} dE}{\int_{E_{min}}^{E_{max}} E^{\alpha} A_{eff}(E, \theta) dE} \quad (9)$$

where $A_{eff}(E, \theta)$ is the effective area calculated in a given multiplicity channel at the fixed zenith angle θ and α is the photon spectral index (see previous section).

In case of no significant excess, typical fluence upper limits to GRB emissions are obtained using the measured counting rates in each of the four multiplicity channels and a model for the GRBs.

Assuming a power law spectrum up to E_{max} ranging from 100 MeV to 1 TeV, no $\gamma\gamma$ absorption by the Extragalactic Background Light, a zenith angle $\theta = 20^\circ$ and a duration $\Delta t = 10$ s, the upper limits corresponding to a 4σ excess in the multiplicity channel 1 are calculated as a function of the spectral

index in the energy range $10 \text{ MeV} - E_{max}$. The results are reported in Figure 10. For different time durations, upper limits scale as $\sqrt{\Delta t(s)}/10$.

In order to evaluate the real possibilities of a GRB detection, we compare the ARGO-YBJ sensitivity with the GRB fluxes measured by EGRET. During its lifetime EGRET detected 16 events at energies $>200 \text{ MeV}$ [1]. Above this energy, all their spectra show a power law behaviour without any cutoff, suggesting the possibility that a large part of GRBs could emit GeV or even TeV gamma rays.

In our simple model every EGRET GRB spectrum is extrapolated to higher energies, using the measured power law index, up to a maximum energy E_{max} representing a possible intrinsic cutoff at the source. Then we consider an exponential cutoff to take into account the effects of the extragalactic absorption, obtaining the spectrum: $dN/dE = K E^\alpha e^{-\tau(E,z)}$. The intrinsic energy cutoff is assumed in the range $100 \text{ GeV} < E_{max} < 1 \text{ TeV}$ and the GRB redshift in the range $0 \leq z \leq 3$. The absorption factor is calculated by using the values of optical depth $\tau(E, z)$ given in [23].

Our calculation shows that a fraction ranging from 10% to 50% of EGRET GRBs is above the ARGO-YBJ minimum detectable flux, depending on the cutoff energy E_{max} and the redshift z of the GRB. Assuming $E_{max}=1 \text{ TeV}$ ($E_{max}=100 \text{ GeV}$) and no absorption of gamma rays, ARGO-YBJ could detect 50% (30%) of EGRET GRBs. If $z=1$ ($z=3$) this value reduces to $\sim 20\%$ (10%), for both values of E_{max} . Considering that EGRET observed 16 GRBs during 7 years (1991-1997) and that the EGRET field of view ($\sim 0.5 \text{ sr}$) is about four times smaller than that of the present Swift satellite, ~ 9 GRBs similar to those seen by EGRET are expected to occur in one year in the Swift field of view.

Since about 1/10 of these bursts are, by chance, in the ARGO-YBJ field of

view, we expect ~ 1 EGRET-like GRB detected by Swift to occur in our detector field of view in one year. A fraction of them (depending on z and E_{max}) will be effectively detectable.

6 Conclusions

The ARGO-YBJ detector operated in scaler mode has a high duty cycle and optimal stability, fulfilling the fundamental requirements of the scaler mode technique.

The main goal is the measurement of the high energy tail of GRB spectra, and the detection of few events during the experiment life time is expected if the spectrum of the most energetic GRBs extends at least up to 100 GeV. In this case, with four measurement channels sensitive to different energies, valuable information on the high energy spectrum slope and possible cutoff may be obtained.

In any case, even if no signal is detected, the large field of view and the high duty cycle, allowing for continuous monitoring overhead, make the ARGO-YBJ experiment one of the most sensitive detectors for the study of the high energy spectrum of GRBs, with typical fluence upper limits down to 10^{-5} erg/cm^2 in the 1 - 100 GeV region, well below the energy range explored by the present generation of Cherenkov telescopes.

On the other hand, due to the high rigidity cut-off, the large area of the detector and its high mountain location allow the study of the solar modulation of galactic cosmic rays and energetic relativistic particles coming from the Sun with high sensitivity and fine time resolution. This has been shown by the observation of the January 2005 FD with a preliminary discussion on the

recovery phase.

Data collected up to May 2008 have been analyzed according to the procedures outlined in this work and the results of these analyses will be presented in later papers.

7 Acknowledgements

This paper is supported in part by the National Natural Science Foundation of China (NSFC) under the grant No. 10120130794, the Chinese Ministry of Science and Technology, the Key Laboratory of Particle Astrophysics, Institute of High Energy Physics (IHEP), Chinese Academy of Science (CAS) and the National Institute of Nuclear Physics of Italy (INFN).

The authors thank M. Storini for useful discussion, M. Dattoli also thanks the National Institute of Astrophysics of Italy (INAF) for partly supporting her activity in this work.

References

- [1] J.R. Catelli et al., in “*Gamma Ray Bursts*”, edited by C.A. Meegan, AIP Conf. Proc. No. 428, p.309 (AIP, New York, 1997).
- [2] K. Hurley et al., *Nature* 372 (1994) 652.
- [3] S. Vernetto, *Astrop. Phys.* 13 (2000) 75.
- [4] G. Aielli et al., *Nucl. Instr. and Meth. A* 562 (2006) 92.
- [5] X. Sheng et al., in: *Proceedings of the 29th ICRC*, vol. 5, 2005, p. 151.
- [6] D. Malan and H. Moraal, *South African Journal of Science* 98 (2002) 1.

- [7] L. Dorman, “*Cosmic Rays in the Earth atmosphere and Underground*”, Astrophysics and Space Science Library, vol. 303, Kluwer Academic Publishers, 2004.
- [8] A.M. Hillas, in “*Cosmic Rays*”, p. 50, Oxford: Pergamon Press.
- [9] R. Arnaldi et al., Nucl. Instr. and Meth. A 456 (2000) 140.
- [10] M. Abbrescia et al., Nucl. Instr. and Meth. A 359 (1995) 603.
- [11] R.M. Jacklyn, S.P. Duggal and M.A. Pomerantz, Nature 223 (1969) 601.
- [12] A. Cappa et al., in: Proceedings of the 30th ICRC, SH 3.4, 2007 (in press).
- [13] E.O. Flückiger, R. Bütikofer, M.R. Moser and L. Desorgher in: Proceedings of the 29th ICRC, vol. 1, 2005, p.225.
- [14] J.W. Bieber et al., in: Proceedings of the 29th ICRC, vol. 1, 2005, p.237.
- [15] M. Storini, D.F. Smart and M.A. Shea, in: Proceedings of the 27th ICRC, 2001, p. 4106.
- [16] T. Jämsén, I.G. Usoskin, T. Rähkä, I. Sarkamo, G.A. Kovaltsov, Advances in Space Research 40 (2007) 342.
- [17] D. Heck, J. Knapp, J.-N. Capdevielle, G. Schatz, T. Thouw, CORSIKA: a Monte Carlo code to simulate extensive air showers, Forschungszentrum Karlsruhe, Report FZKA 6019, 1998.
- [18] G. Battistoni, C. Bloise, A. Ferrari, M. Monteno, V. Patera, E. Scapparone, Astroparticle Phys. 7 (1997) 101.
- [19] A.A. Abdo et al., Astrophysical Journal 666 (2007) 361.
- [20] B. Wiebel-Sooth, P.L. Biermann and H. Meyer, Astronomy and Astrophysics 330 (1998) 389.

- [21] B.L. Dingus, J.R. Catelli and E.J. Schneid, in: Proceedings of the 25th ICRC, vol. 3, 1997, p. 29.
- [22] T. K. Gaisser & M. Honda, Ann. Rev. Nucl. Part. Sci. 52 (2002) 153.
- [23] T.M. Kneiske, T. Bretz, K. Mannheim, D.H. Hartmann, *A&A* 413 (2004) 807.

8 Captions list

Fig. 1 Experimental distributions of the counting rates and their Gaussian fits for a typical cluster: (a) $C_{\geq 1}$, (b) $C_{\geq 2}$, (c) $C_{\geq 3}$ and (d) $C_{\geq 4}$ for 30 minutes data accumulation. The standard deviation of the Gaussian fit (σ_{exp}) is compared with the square root of the mean of the experimental distribution (σ_{th}) to check the compatibility with the Poisson distribution.

Fig. 2 Experimental distributions of the counting rates and their Gaussian fits for a typical cluster: (a) C_1 , (b) C_2 and (c) C_3 for 30 minutes data accumulation. The standard deviation of the Gaussian fit (σ_{exp}) is compared with the square root of the mean of the experimental distribution (σ_{th}) to check the compatibility with the Poisson distribution.

Fig. 3 Experimental distribution of the total number of particles hitting a typical cluster and its Gaussian fit for 30 minutes data accumulation. The standard deviation of the Gaussian fit (σ_{exp}) is compared with the expected value derived from the single multiplicities counting rates (see text, eq. (3)).

Fig. 4 Experimental distribution of the normalized excesses of signal over background of a typical cluster (see text, eq. (5)) compared with a Gaussian fit. Top: $C_{\geq 1}$ channel; bottom: sum of the four channels.

Fig. 5 Counting rates as a function of time for 3 clusters for multiplicities from ≥ 1 to ≥ 4 and 72 hours of data accumulation, together with pressure (P) and RPC temperature (T) behaviour for the same time interval (lower plots).

Fig. 6 Experimental distributions of counting rates for $C_{\geq 1}$ and $C_{\geq 2}$ of a typical cluster before (left) and after (right) corrections for pressure and RPC temperature in a period of 24 hours. The standard deviation of the Gaussian fit (σ_{exp}) is compared with the square root of the mean of the experimental

distribution (σ_{th}) and the resulting “non-Poissonian” behaviour $\frac{\Delta\sigma}{\sigma} = \frac{\sigma_{exp}-\sigma_{th}}{\sigma_{exp}}$ is reported.

Fig. 7 Plot of the YBJ neutron monitor (NM) data compared with the four counting rate distributions (added on all the operating 12 clusters and corrected only for the atmospheric pressure) during the Forbush Decrease of January 2005 (Neutron Monitor data: courtesy of the Yangbajing Neutron Monitor Collaboration).

Fig. 8 Effective areas for photon and proton-induced showers (left and right plot, respectively) with zenith angle $\theta = 20^\circ$ in the four multiplicity channels (from top to bottom, 1, 2, 3 and ≥ 4).

Fig. 9 Convolutions of the effective areas of Fig. 8 with a differential power law spectrum of index $\alpha = -2.0$ for photons and $\alpha = -2.77$ for protons, taking into account in this latter case the geomagnetic bending, in the four multiplicity channels (from top to bottom, 1, 2, 3 and ≥ 4).

Fig. 10 Fluence upper limits in the energy range 10 MeV - E_{max} corresponding to a 4σ excess in the multiplicity channel 1, as a function of the GRB spectral index, for a zenith angle $\theta=20^\circ$, a time duration $\Delta t = 10$ s and a redshift $z=0$. Each set of points refers to different E_{max} as shown in the figure.

9 Figures

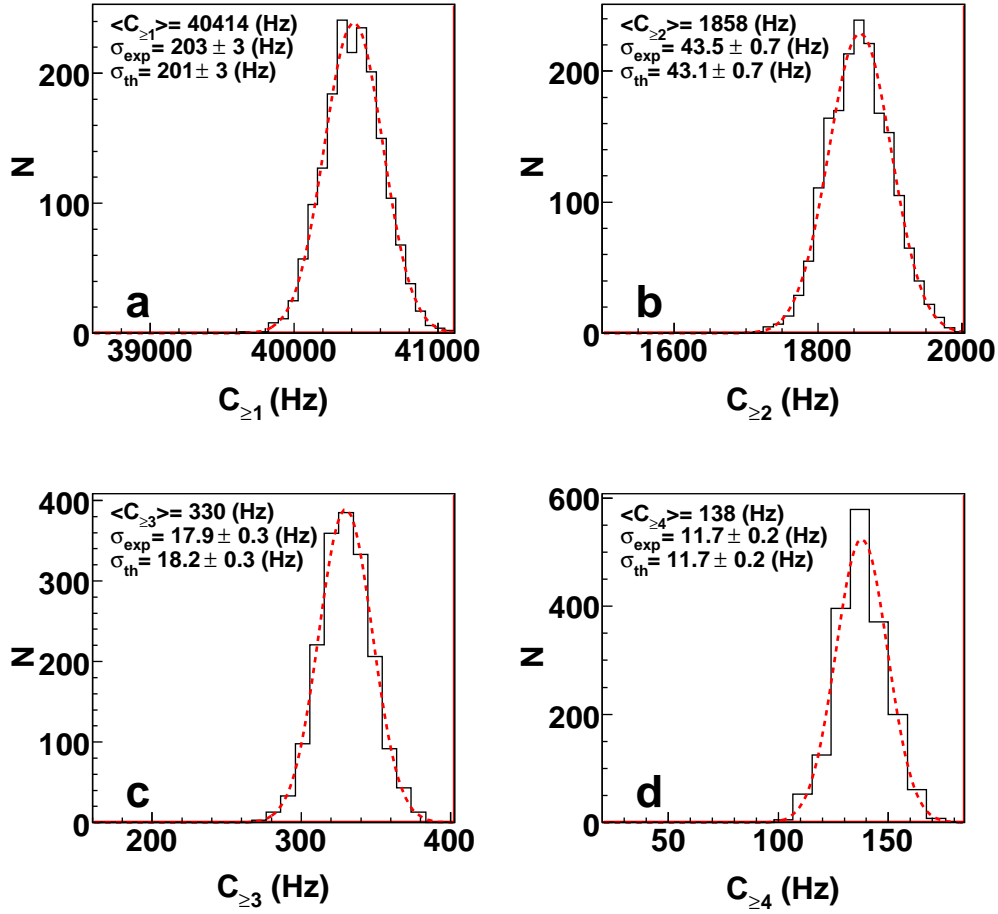


Fig. 1. Experimental distributions of the counting rates and their Gaussian fits for a typical cluster: (a) $C_{\geq 1}$, (b) $C_{\geq 2}$, (c) $C_{\geq 3}$ and (d) $C_{\geq 4}$ for 30 minutes data accumulation. The standard deviation of the Gaussian fit (σ_{exp}) is compared with the square root of the mean of the experimental distribution (σ_{th}) to check the compatibility with the Poisson distribution.

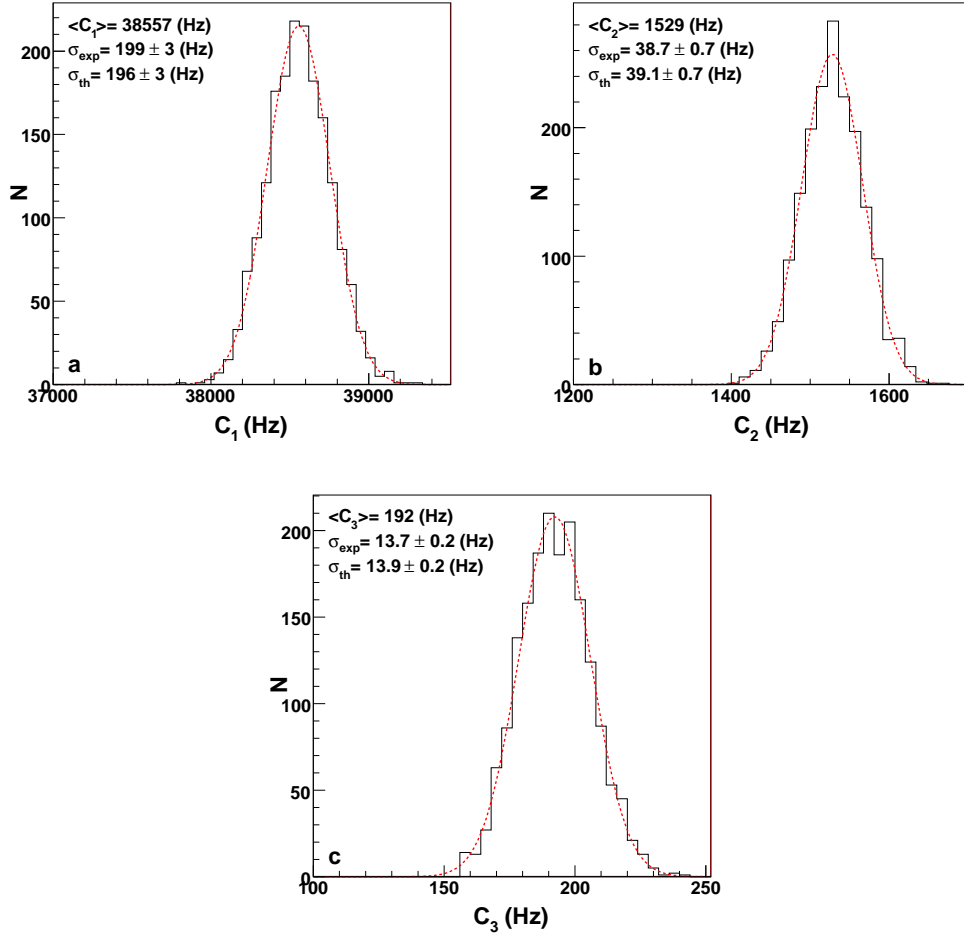


Fig. 2. Experimental distributions of the counting rates and their Gaussian fits for a typical cluster: (a) C_1 , (b) C_2 and (c) C_3 for 30 minutes data accumulation. The standard deviation of the Gaussian fit (σ_{exp}) is compared with the square root of the mean of the experimental distribution (σ_{th}) to check the compatibility with the Poisson distribution.

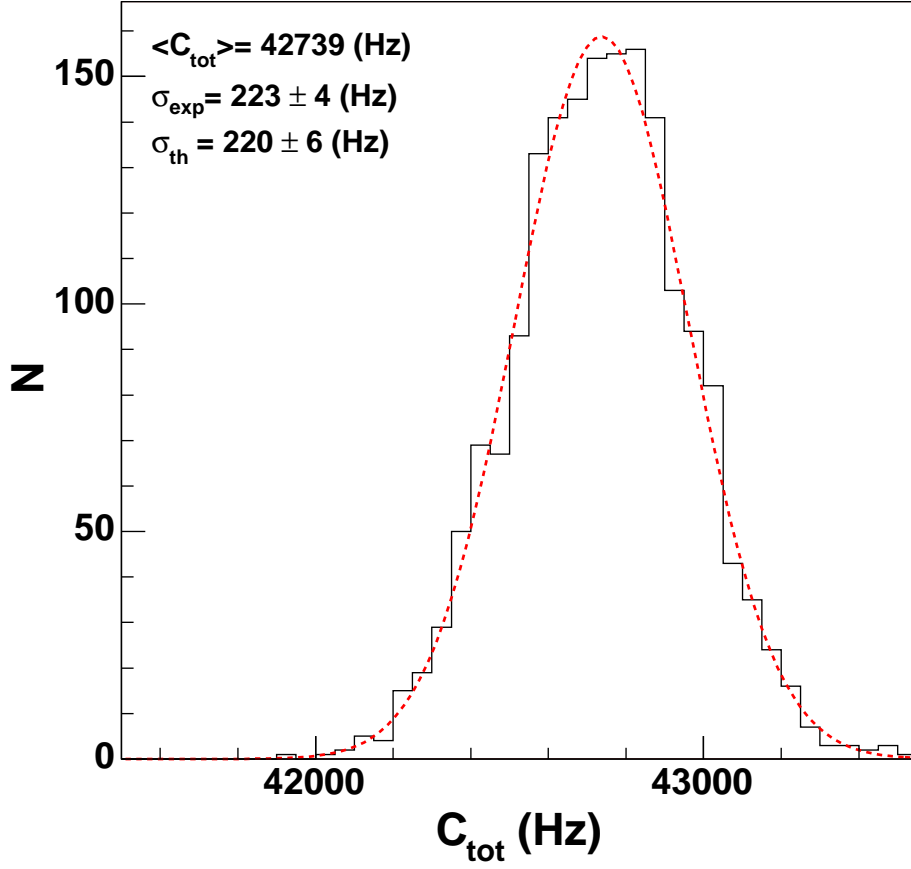


Fig. 3. Experimental distribution of the total number of particles hitting a typical cluster and its Gaussian fit for 30 minutes data accumulation. The standard deviation of the Gaussian fit (σ_{exp}) is compared with the expected value derived from the single multiplicities counting rates (see text, eq. (3)).

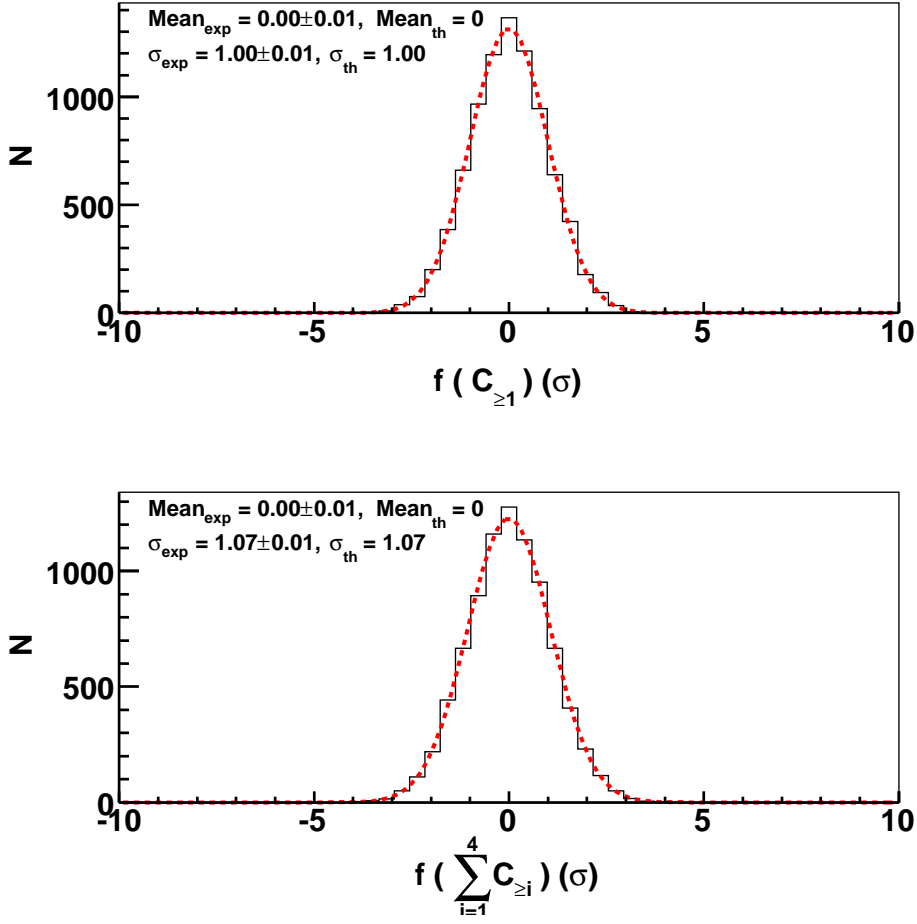


Fig. 4. Experimental distribution of the normalized excesses of signal over background of a typical cluster (see text, eq. (5)) compared with a Gaussian fit. Top: $C_{\ge 1}$ channel; bottom: sum of the four channels.

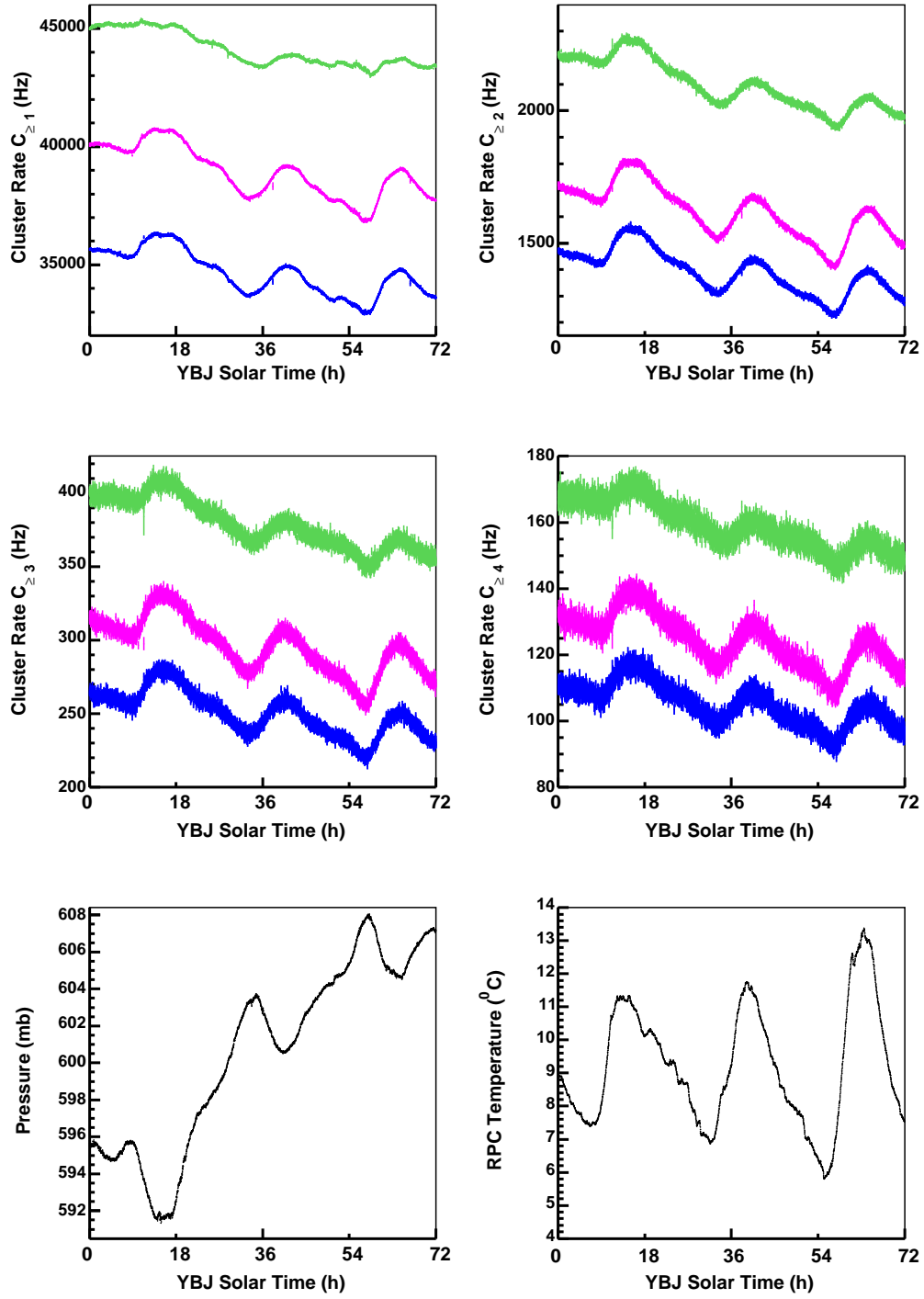


Fig. 5. Counting rates as a function of time for 3 clusters for multiplicities from ≥ 1 to ≥ 4 and 72 hours of data accumulation, together with pressure (P) and RPC temperature (T) behaviour for the same time interval (lower plots).

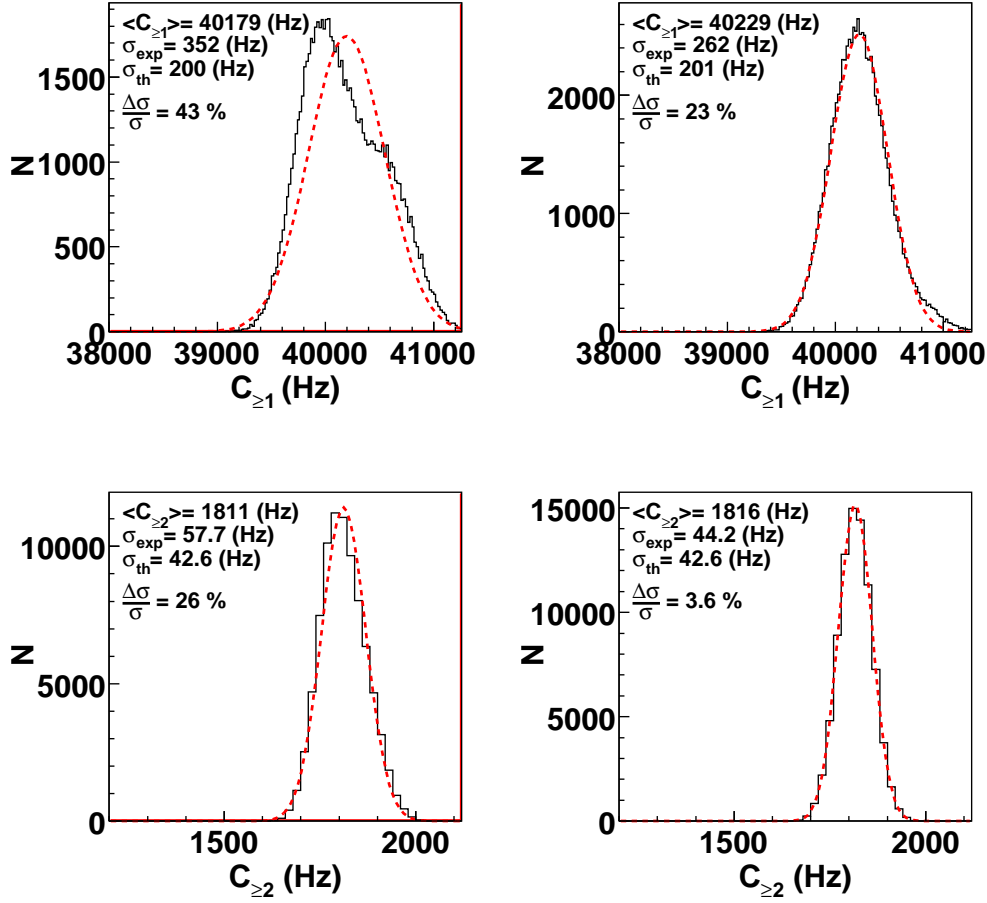


Fig. 6. Experimental distributions of counting rates for $C_{\geq 1}$ and $C_{\geq 2}$ of a typical cluster before (left) and after (right) corrections for pressure and RPC temperature in a period of 24 hours. The standard deviation of the Gaussian fit (σ_{exp}) is compared with the square root of the mean of the experimental distribution (σ_{th}) and the resulting “non-Poissonian” behaviour $\frac{\Delta\sigma}{\sigma} = \frac{\sigma_{exp} - \sigma_{th}}{\sigma_{exp}}$ is reported.

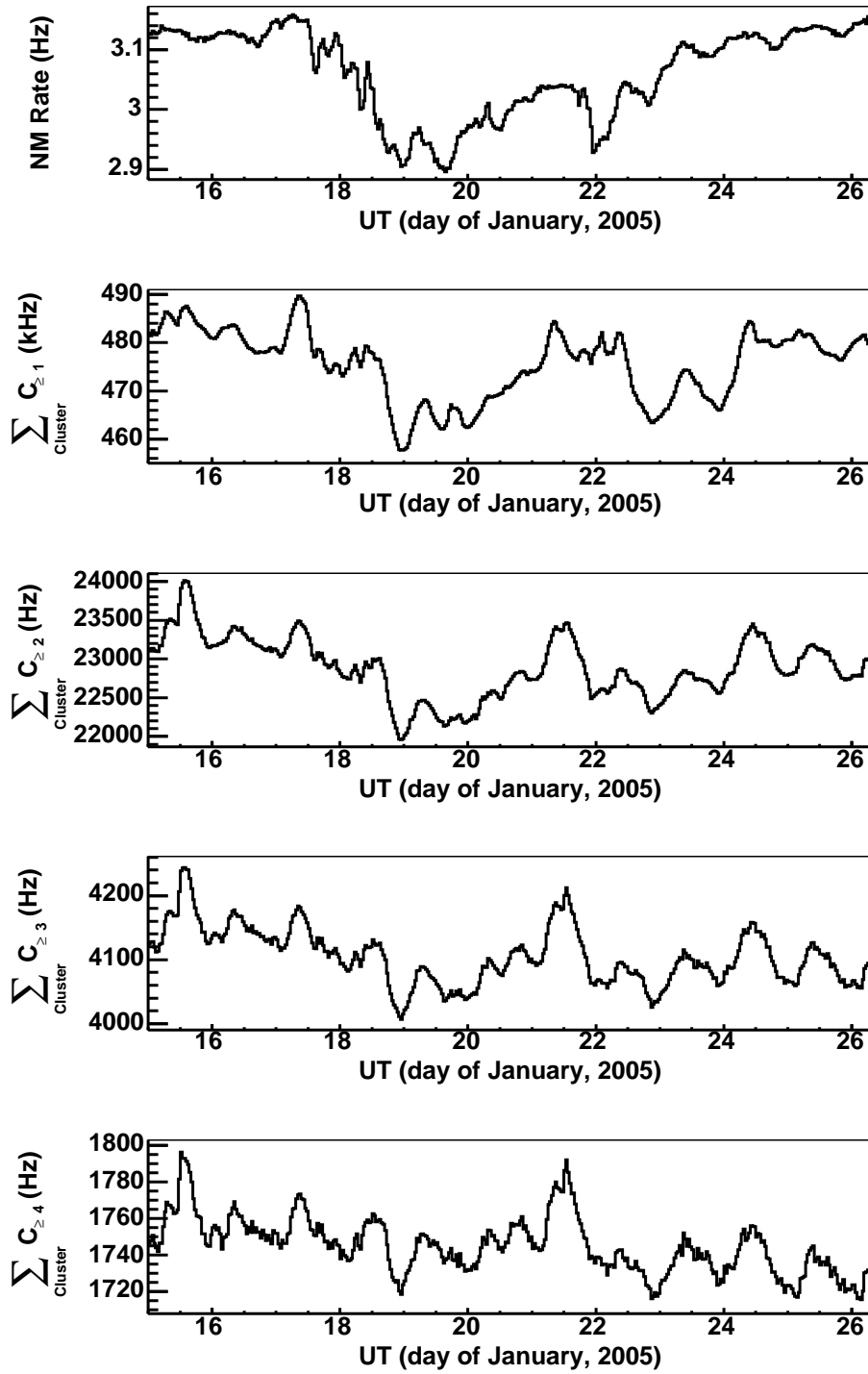


Fig. 7. Plot of the YBJ neutron monitor (NM) data compared with the four counting rate distributions (added on all the operating 12 clusters and corrected only for the atmospheric pressure) during the Forbush Decrease of January 2005 (Neutron Monitor data: courtesy of the Yangbajing Neutron Monitor Collaboration).

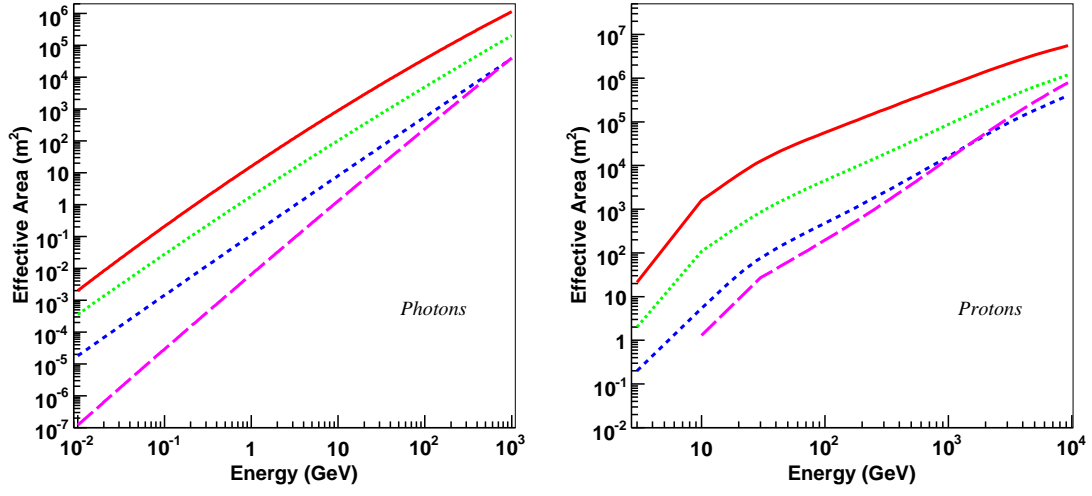


Fig. 8. Effective areas for photon and proton-induced showers (left and right plot, respectively) with zenith angle $\theta = 20^\circ$ in the four multiplicity channels (from top to bottom, 1, 2, 3 and ≥ 4).

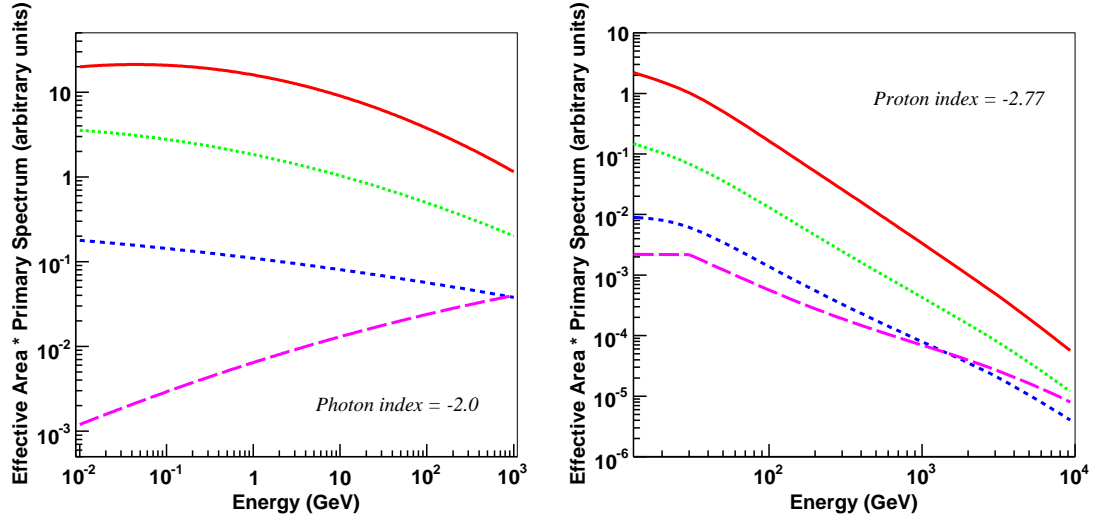


Fig. 9. Convolutions of the effective areas of Fig. 8 with a differential power law spectrum of index $\alpha = -2.0$ for photons and $\alpha = -2.77$ for protons, taking into account in this latter case the geomagnetic bending, in the four multiplicity channels (from top to bottom, 1, 2, 3 and ≥ 4).

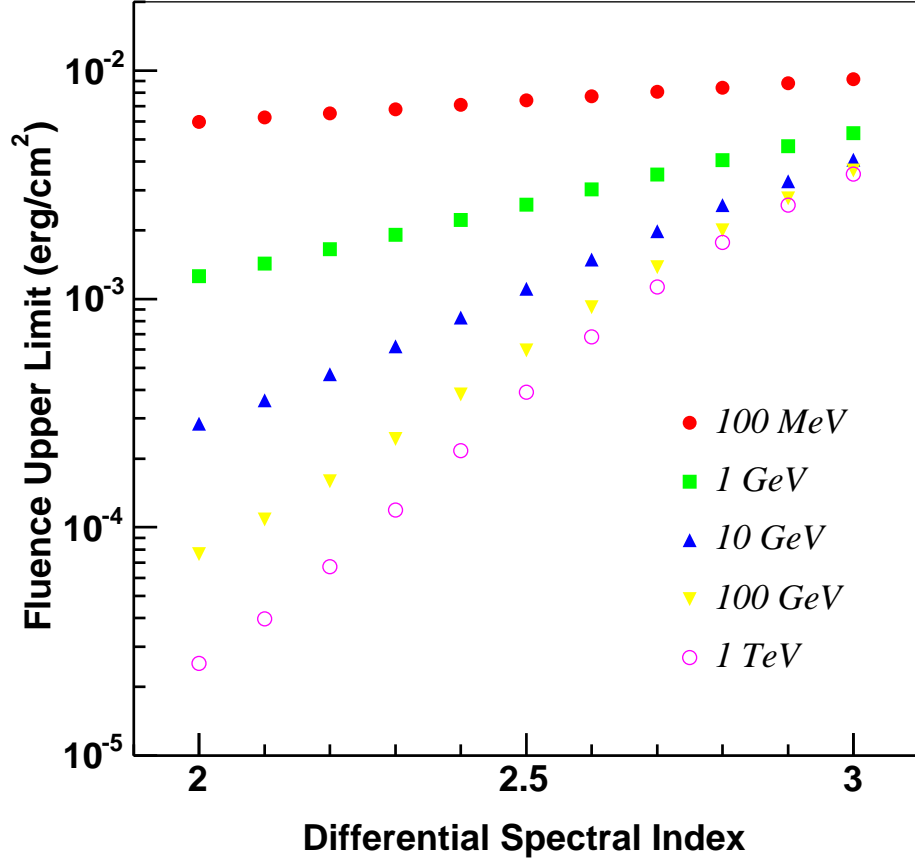


Fig. 10. Fluence upper limits in the energy range 10 MeV - E_{max} corresponding to a 4σ excess in the multiplicity channel 1, as a function of the GRB spectral index, for a zenith angle $\theta=20^\circ$, a time duration $\Delta t = 10$ s and a redshift $z=0$. Each set of points refers to different E_{max} as shown in the figure.